Molecular Accessibility and Diffusion of Resorufin in Zeolite Crystals

J. J. Erik Maris+,[a, d] Luke A. Parker+,[a, c] Katarina Stanciakova,[a] Nikolaos Nikolopoulos,[a] Koen M. H. Berendsen,[a] Alfons van Blaaderen,[b] Florian Meirer,[a] Freddy T. Rabouw,[a, b] and Bert M. Weckhuysen*[a]

We have used confocal laser scanning microscopy on the small, fluorescent resorufin dye molecule to visualize molecular accessibility and diffusion in the hierarchical, anisotropic pore structure of large (~10 μm-sized) zeolite-β crystals. The resorufin dye is widely used in life and materials science, but only in its deprotonated form because the protonated molecule is barely fluorescent in aqueous solution. In this work, we show that protonated resorufin is in fact strongly fluorescent when confined within zeolite micropores, thus enabling fluorescence microimaging experiments. We find that J-aggregation guest–guest interactions lead to a decrease in the measured fluorescence intensity that can be prevented by using non-fluorescent spacer molecules. We characterized the pore space by introducing resorufin from the outside solution and following its diffusion into zeolite-β crystals. The eventual homogeneous distribution of resorufin molecules throughout the zeolite indicates a fully accessible pore network. This enables the quantification of the diffusion coefficient in the straight pores of zeolite-β without the need for complex analysis, and we found a value of $3\times10^{-15}\,\mathrm{m^2\,s^{-1}}$. Furthermore, we saw that diffusion through the straight pores of zeolite-β is impeded when crossing the boundaries between zeolite subunits.

Introduction

Zeolites are industrially important porous materials as their microporosity allows for shape-selective catalysts.[1–3] One of the industrially most applied zeolites is zeolite-β. It has numerous applications in the production of fine chemicals as well as in the petrochemical industry, often as a catalyst for alkylation and transalkylation reactions.[2,4,5] Mass transport is often the limiting step in its application because of the strong interaction between guest molecules and the micropore walls of the zeolite host material.[6–9] Therefore, the rational design of even more efficient zeolite materials requires careful characterization of their pore network and better understanding of mass transport therein, including the involved intricate host–guest chemistry and physics.

Zeolite-β has the BEA framework constituting intersecting 6.6×6.7 Å straight channels along the crystallographic *a*- and *b*-axes. These channels are built from rings of twelve tetrahedra, classifying zeolite-β as a large-pore zeolite.[2,10] Along the crystallographic *c*-axis, well-defined sinusoidal channels with a size of 5.6×5.6 Å and zigzag shape are present in the ordered polymorph A, whereas these channels are randomly shaped in the disordered zeolite.[11–13] Regardless of the (dis)order along the crystallographic *c*-axis, uniform straight channels are formed in the zeolite. The channels in the *a*-, *b*-, and *c*-directions are interconnected, creating an anisotropic, three-dimensional pore network.[10,11,14,15] Thus, consideration of the pore anisotropy when investigating molecular diffusion and the pore structure is essential for the improvement of zeolite-β and other microporous materials.

The advent of micro-imaging techniques, notably interference microscopy and infrared micro-imaging, has enabled direct measurements of mass transport and molecular diffusion barriers on the single-zeolite-crystal level.[6,16,17] Cuboid crystal shapes and symmetries are preferred for these micro-imaging techniques as the concentration of diffusing molecules is only obtained as a two-dimensional projection image.[17] Diffusion in more complex zeolite crystal shapes, such as zeolite-β's truncated bipyramid

[a] Dr. J. J. Erik Maris,+ Dr. L. A. Parker,+ Dr. K. Stanciakova, Dr. N. Nikolopoulos, K. M. H. Berendsen, Dr. F. Meirer, Dr. F. T. Rabouw, Prof. B. M. Weckhuysen
     Inorganic Chemistry and Catalysis Group
     Utrecht University
     Debye Institute for Nanomaterials Science and
     Institute for Sustainable and Circular Chemistry
     Universiteitsweg 99, 3584 CG Utrecht (The Netherlands)
     E-mail: B.M.Weckhuysen@uu.nl

[b] Prof. A. van Blaaderen, Dr. F. T. Rabouw
     Soft Condensed Matter Group, Utrecht University
     Debye Institute for Nanomaterials Science
     Princetonplein 1, 3584 CC Utrecht (The Netherlands)

[c] Dr. L. A. Parker+
     TNO
     Princetonlaan 6, 3584 CB Utrecht (The Netherlands)

[d] Dr. J. J. Erik Maris+
     Optical Materials Engineering Laboratory, ETH Zürich
     Leonhardstrasse 21, 8092 Zürich (Switzerland)

[+] These authors contributed equally to this work.

⊡ Supporting information for this article is available on the WWW under https://doi.org/10.1002/chem.202302553

shape, can only be interpreted straightforwardly when the concentration is imaged in three dimensions. Confocal laser scanning microscopy (CLSM) can accomplish this provided that proper fluorescent diffusing molecules are available. Even information about the fluorescent molecule's microenvironment, such as polarity and pH, can be inferred directly from its emission spectrum.[18,19] Nonetheless, reports of CLSM used for the visualization of diffusion in microporous solids or their microenvironment are relatively scarce[20,21] because most fluorescent molecules are larger than typical zeolite pores (e.g., rhodamine dyes), prohibiting them from entering and probing the local chemistry in the micropore structure.

Resorufin is a promising fluorescent dye because it is sufficiently small to enter zeolite pores and has favorable photophysical properties. The molecule has a pK_a of 5.8 in water, meaning that above pH 5.8 most molecules exist in free solution in a deprotonated, anionic form (Figure 1a). This form of resorufin is used for fluorescence assays in biology and catalysis[7,8,22–27] because of its long excitation and emission wavelength, high fluorescence quantum yield, large molar absorptivity, and good stability against light irradiation and pH changes.[28–30] Below pH 5.8 resorufin exists in aqueous solution predominantly as neutral, protonated molecule, which is poorly soluble and only weakly fluorescent,[30] and consequently has not found use as fluorescent probe.

Here, we investigate resorufin as a probe for CLSM microimaging experiments and demonstrate its application in large zeolite-β crystals. Our study starts with the observation that protonated resorufin exhibits bright fluorescence when it is confined in the pores of zeolite-β. The bright fluorescence is affected by guest–host and guest–guest interactions. Both the aggregation behavior and dissociation state of the resorufin are found to affect its fluorescence properties. We identify molecular J-aggregation as the dominant interaction via comparison of experimental microimaging diffusion videos with a model consid-
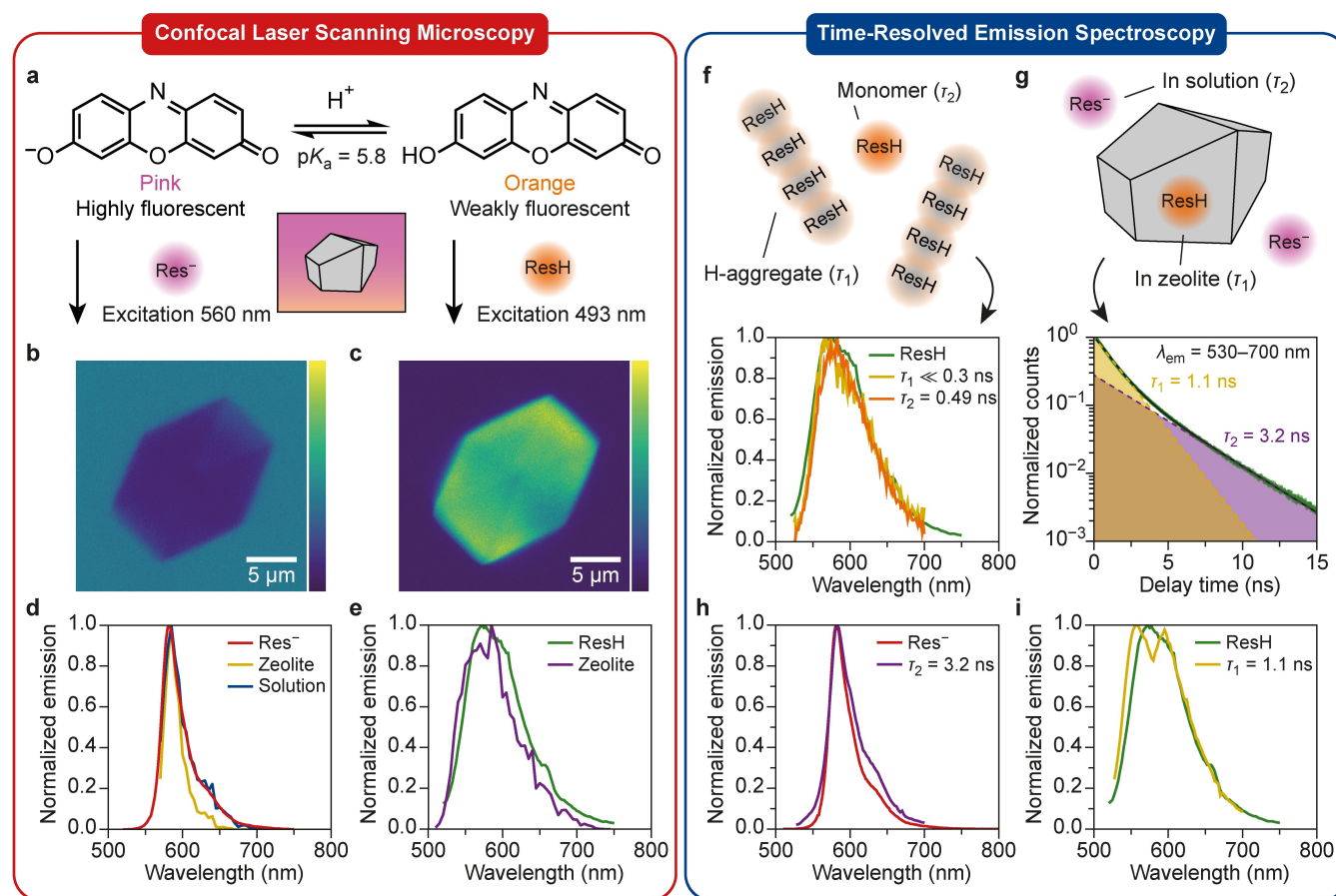

Figure 1. a) Properties of resorufin in basic (left) and acidic (right) aqueous solution. Selective excitation of deprotonated resorufin (Res⁻; b) and protonated resorufin (ResH; c) in and around a zeolite-β crystal incubated for 3 h in a slightly pH-basic resorufin solution. Confocal laser scanning microscopy micrographs recorded with the excitation wavelengths and intensity given in (a). d) Emission spectra in the zeolite and solution from (b) overlaid with a reference spectrum of Res⁻ recorded in aqueous solution. e) Emission spectrum in the zeolite from (c) overlaid with a reference spectrum of ResH recorded in aqueous solution. f) Normalized emission spectra of the $\tau_1 \ll 0.3$ ns (smoothed by a 25 nm moving average) and $\tau_2 = 0.49$ ns components of protonated resorufin (ResH) overlaid with a reference emission spectrum of ResH recorded in aqueous solution. g) Decay curve of the fluorescence from an aqueous slurry of resorufin-stained zeolite-β averaged over the detection wavelengths 530–700 nm (green dots) and a bi-exponential fit (solid black line). The decay components $\tau_1 = 1.1$ ns (yellow) and $\tau_2 = 3.2$ ns (purple) of the fit are indicated by the dashed lines. Normalized emission spectra of the $\tau_2 = 3.2$ ns (h) and $\tau_1 = 1.1$ ns (i) components overlaid with the reference emission spectra of Res⁻ and ResH recorded in aqueous solution, respectively.

Chemistry–A European Journal

Research Article
doi.org/10.1002/chem.202302553

Chemistry Europe
European Chemical
Societies Publishing

ering the relevant guest–host and guest–guest interactions. Finally, the accessibility of the zeolite's pore network as well as the molecular diffusivity into the pores are studied in conditions where J-aggregation is suppressed.

Results and Discussion

Resorufin for microimaging experiments

In a typical CLSM micro-imaging experiment, we introduce an aqueous solution of deprotonated resorufin (Res$^-$) dye to ~10 μm-sized zeolite-β crystals suspended in water (material characterization in Section S3 in the Supporting Information). Here, barely any fluorescence signal from inside the zeolite crystal is observed for excitation wavelengths around the absorption maximum of Res$^-$ (Figures 1b and S3). The measured weak signal is consistent with deprotonated Res$^-$ in Figure 1d. Surprisingly, we observe the strongest fluorescence signal inside the zeolite when excited at 493 nm, which corresponds to the absorption maximum of neutral resorufin, ResH (Figures 1c and S3). The emission spectrum matches the ResH reference spectrum in Figure 1e and confirms that ResH instead of Res$^-$ is the dominant fluorescent species inside the zeolite near neutral pH, despite its weak fluorescence in aqueous solution.

The ResH fluorescence intensity inside the zeolite (Figure 1c) is higher than that of Res$^-$ in solution (Figure 1b) when excited with the same intensity at their respective absorption maximum. This demonstrates that zeolite-confined ResH, similarly to Res$^-$ in aqueous solution, possesses good optical properties for a fluorescent probe, including a relatively large molar absorptivity and/or high fluorescence quantum yield. Direct comparison with the brightness of Res$^-$ per molecule is not possible in this experiment, because the concentration of ResH inside the zeolite is unknown.

We further investigated ResH fluorescence inside the zeolite and in homogeneous aqueous solution through the excited-state fluorescence lifetime. A lifetime of 3.0 ns is found for Res$^-$ in aqueous solution; however, a completely different picture emerges for ResH. We find two lifetime components in water ($\tau_1 \ll 0.3$ and $\tau_2 = 0.49$ ns), while one would expect only a single component for a single fluorescent species in solution (Section S4). We assign this extra component to molecular aggregation.

Ultraviolet–visible spectroscopy in combination with density functional theory (DFT) computations reveal that ResH predominantly forms H-aggregates in solution (Sections S5.1, S5.2). The lifetime of H-aggregates is known to be shorter because of efficient non-radiative pathways that are available when the molecules are in close contact, resulting in weak fluorescence.[31–33] We reconstruct the emission spectra of the $\ll 0.3$-ns and 0.49-ns lifetime components to identify their molecular origin. Because the lifetime components have a similar emission spectrum identical to ResH, it can be concluded that both originate from ResH, either from monomeric molecules (0.49 ns) or aggregates ($\ll 0.3$; Figure 1f).

We employ a similar approach to investigate resorufin's fluorescence inside the zeolite. The lifetime in an aqueous slurry of resorufin-stained zeolite-β is probed using 510 nm excitation, which allows for simultaneous excitation of Res$^-$ and ResH (see excitation spectra in Figure S3). Upon confinement of some of the dye within the zeolite, two different fluorescent species are present resulting in a biexponential decay with lifetime components of $\tau_1 = 1.1$ and $\tau_2 = 3.2$ ns (Figure 1g). The reconstructed emission spectrum of the $\tau_1 = 1.1$-ns component matches the emission spectrum of ResH (Figure 1h),[29,34] while the spectrum of the 3.2-ns lifetime component is in agreement with the spectrum of aqueous Res$^-$ (Figure 1i). No $\tau \ll 0.3$-ns lifetime component is found for resorufin confined in the zeolite, showing that aggregation-induced quenching is suppressed inside the zeolite micropores at these concentrations, which leads to enhanced ResH fluorescence with respect to aqueous solution.

We compare the fluorescence lifetimes obtained from resorufin confined in the zeolite with references recorded in aqueous solution. The fluorescence lifetime of Res$^-$ increases marginally from 3.0 to 3.2 ns in the presence of a zeolite material, probably because Res$^-$ is mostly in aqueous solution. Importantly, the fluorescence lifetime of monomeric ResH increases through interaction with the zeolite, from 0.49 to 1.10 ns, resulting in enhanced fluorescence. Similar enhancements in fluorescence via the quantum yield have been observed for the dye pyronine Y, when strongly confined within microporous MgAPO crystals, as a result of the rigidity imposed on the dye molecule by the micropores.[33] Based on these observations, we expect that monomeric ResH is stabilized inside the zeolite micropores resulting in brighter ResH fluorescence upon confinement.

Guest–guest and guest–host interactions

To understand and use resorufin as a fluorescent probe in zeolite materials, we first characterize the interactions that affect ResH fluorescence inside the zeolite. Therefore, the acid dissociation equilibrium of resorufin confined inside the pores of zeolite-β as a function of the pH in external solution is investigated first. We measure the fluorescence emission spectrum after 45 min incubation of the zeolite in a pH 7 aqueous solution of resorufin. Here, we record the emission spectrum of ResH excited close to its absorption maximum (Figure 2a). The formation of ResH species inside the zeolite at near neutral solution pH, which is ~1 pH point above resorufin's pK_a, indicates that the pH inside the zeolite is more acidic than in the solution outside. Addition of extra ammonia base to reach pH 9 in solution, then followed by 35 min incubation, results in the loss of the ResH emission spectrum inside the zeolite. Instead, we measure the emission spectrum of Res$^-$, even when we excite close to ResH's absorption maximum (Figure 2b). We find that an increase in the external pH from 7 to 9 leads to ResH deprotonation inside the zeolite. Thus, the fluorescence signal from ResH is decreased when the pH in the external solution is sufficiently high.
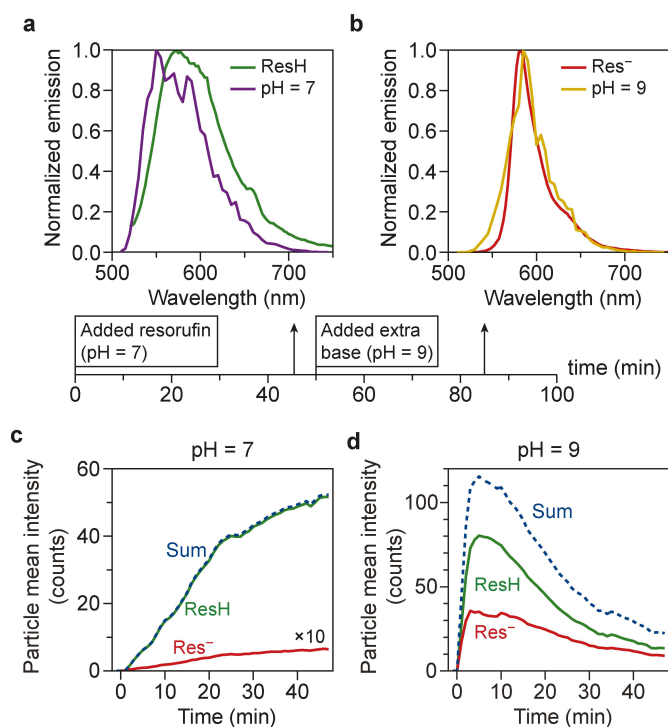
Chemistry–A European Journal

Research Article
doi.org/10.1002/chem.202302553

**Chemistry
Europe**
European Chemical
Societies Publishing

Figure 2. a) Fluorescence emission spectra of resorufin inside a zeolite-β crystal ($\lambda_{ex} = 493$ nm) soaked in water, followed by incubation in ~10 nM ammonia (corresponding to pH 7) and 50 μM resorufin starting at time = 0 min. The fluorescence emission spectrum after 45 min (purple) is compared to a reference spectrum of protonated ResH (green). b) Fluorescence emission spectrum of the same sample as in (a), but incubated for another 35 min in ~5 μM ammonia (corresponding to pH 9), compared to a reference spectrum of deprotonated Res⁻. Total intensity as a function of time inside two different H-zeolite-β crystals after incubation in an ammonia solution at pH 7 (c) or 9 (d) and 50 μM resorufin. Excitation wavelengths of 493 and 560 nm enabled the selective excitation of ResH and Res⁻, respectively. For clarity, the signal from the 560 nm excitation in (c) is multiplied by 10. The fluorescence emission in (a)–(d) was recorded from within the center plane of the zeolite by using confocal laser scanning microscopy.

We further investigate the effect of the solution pH on the measured fluorescence intensity in two different crystals, incubated in a resorufin solution of pH 7 or 9 (Figure 2c, d). Here, the acid dissociation of resorufin is followed by exciting close to the absorption maximum of ResH ($\lambda_{ex} = 493$ nm) or Res⁻ ($\lambda_{ex} = 560$ nm) and recording the fluorescence emission. Based on the UV-Vis absorption spectra of the molecules, cross-excitation of Res⁻ at 493 nm and ResH at 560 nm excitation wavelengths can occur to a slight degree (Figure S3). In Figure 2c, the temporal evolution of the ResH and Res⁻ fluorescence intensity inside a single zeolite-β crystal is shown at solution pH 7. The Res⁻ fluorescence intensity is low compared to the ResH intensity at solution pH 7, and the Res⁻ signal is likely a result of cross-excitation of ResH (note the 10× magnification of the Res⁻ signal). The intensity profile of ResH has not yet reached a maximum or plateau after 45 min. At solution pH 9, both ResH and Res⁻ are present simultaneously within the zeolite (Figure 2d). In contrast to the filling at pH 7, the intensity profile of ResH reaches a maximum within 10 min at pH 9. Interestingly, the summed intensity decreases steadily

after its peak, and the loss in ResH or Res⁻ is not compensated by gain of the conjugate dissociation state. This indicates that the measured resorufin fluorescence intensity inside the zeolite crystal is sensitive to another, more dominant process in addition to the local pH.

As we will see below, the decrease in overall fluorescence in the zeolite is a result of aggregation-induced quenching at high concentrations. To explore this, the enthalpy of ResH aggregation inside the straight pores of zeolite-β is computed with DFT. The same types of dimer aggregates as in aqueous solution are considered, and their structures are shown in Figure S10. In contrast to aggregation in aqueous solution, H-stacking is always unfavored, with an endothermic reaction energy of >10 kJ mol⁻¹, showing that the straight channels are not large enough to accommodate H-dimers. However, J-type aggregation is very favorable leading to the formation of J-dimers in zigzag orientation with a reaction enthalpy of −49.4 and −71.3 kJ mol⁻¹ with respect to two different relative orientations (N–N and N–O). These aggregates are known to quench fluorescence in confinement. Martínez-Martínez et al. reported that fluorescent molecules confined in microporous MgAPO had the highest relative quantum yield when the pore structure prevented close-packed J-aggregates, while the fluorescence intensity decreased when J-aggregation was possible.[33]

ResH J-aggregation in the pores of zeolite-β is further investigated with UV-Vis absorption spectroscopy and DFT calculations. We compare the baseline-corrected absorption spectrum of zeolite-β crystals incubated in an aqueous resorufin solution with the absorption spectrum of monomeric ResH (Figure 3a). The main absorption band is red shifted by 20–25 nm with respect to the monomer, while the absorption band at 400 nm remains the same. Moreover, a similar spectral shift and broadening is found for dried and Milli-Q-water-washed samples both incubated in a resorufin solution with pH 7 and 9. The red shift is an indication that ResH J-aggregation occurs within the pores of zeolite-β.

The measured shift in absorbance is compared with time-dependent DFT computations of the J-aggregate UV-Vis absorption spectra shown in Figure 3a, b (see also Section S5.3). The measured red shift of 20–25 nm is larger than the computed 6–15 nm shift as a result of confinement by the zeolite; therefore, the measured shift is likely a result of J-aggregation. Based on the DFT computations, a red shift of 11–27 nm is expected for J-aggregates, which matches our experimental observation. Nevertheless, we must be careful with these assignments as the shifts in absorption wavelength as a result of aggregation are small and the accuracy of the calculations and measurement is limited.

Two alternative explanations for the decrease in intensity are less likely: photobleaching by the laser and the formation of a nonfluorescent covalent dimer. First, we investigate the effect of photobleaching by recording the same field of view at a fast and slow imaging rate, thereby changing the laser exposure (Figure 4a). The intensity decrease is independent of the excitation rate, which shows that the loss of fluorescence intensity is not related to photobleaching. Second, we investigate the condensation reaction of two ResH molecules into a
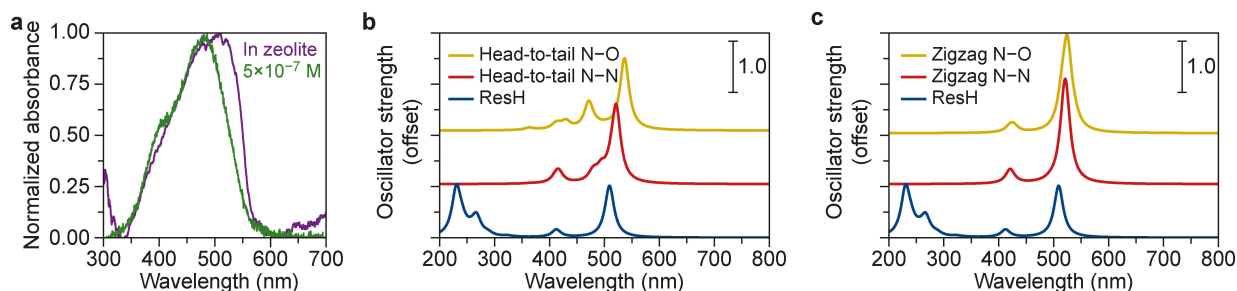
Figure 3. a) Baseline-corrected, normalized UV-Vis absorption spectrum in zeolite-β recorded by microspectroscopy after incubation for 5 min in 100 mM resorufin at pH 9. The spectrum is overlaid with the bulk absorption spectra of protonated resorufin (ResH) in aqueous solution at 5×10^{-7} M. b), c) Simulated UV-Vis absorption spectra of ResH compared with various protonated resorufin ResH J-dimer aggregates. The spectra of head-to-tail J-dimer (b) and zigzag J-dimer (c) with respect to ResH are shown.
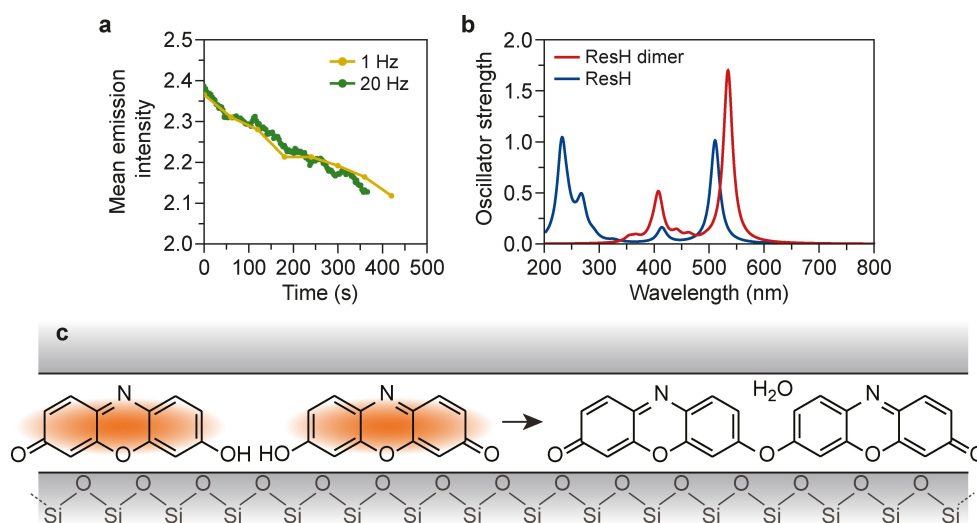

Figure 4. a) Total emission intensity from a H-zeolite-β crystal incubated in Milli-Q water followed by 32 min of incubation in 12.5 mM HEPES (pH 7.4) and 50 μM resorufin ($\lambda_{ex} = 493$ nm). The intensity was recorded from within the center plane of the same crystal at rates of 1 and 20 Hz by using confocal laser scanning microscopy. Because the 20 Hz series was recorded after the 1 Hz series, it is multiplied by 1.19 to overlay the curves. At both imaging rates, the decrease in mean intensity is similar. This indicates that resorufin photobleaching due to laser exposure is not a dominant factor in the observed fluorescence intensity decrease over time. b) Simulated UV-Vis absorption spectra of protonated resorufin compared with a covalent resorufin dimer. c) Schematic representation of the condensation reaction forming a covalent dimer.

non-fluorescent covalent dimer (Figure 4c). Alkylation of the 7-hydroxy group of resorufin such as in the covalent dimer, is expected to result in the quenching of the resorufin fluorescence.[22,35] Our DFT calculations show that the condensation reaction is very endothermic and has a reaction enthalpy of $+71.2$ kJ mol^{-1}. Therefore, it seems unlikely that the large intensity decrease can be explained by this pathway. Nevertheless, the simulated UV-Vis absorption spectrum of the dimer in the zeolite contains a main adsorption peak around 534 nm with another band at 400 nm, which is similar to the measured experimental UV-Vis absorption spectrum in zeolite-β (compare the simulated red-shift in Figure 4b with the experimental one in Figure 3a). Thus, it cannot be excluded that small fractions of a covalent dimer are formed. Considering these factors, a decrease in fluorescent intensity due to J-aggregation inside zeolite-β is the most plausible explanation for the observed ResH fluorescence intensity.

Interactions studied through the filling profile

The different resorufin filling profiles at solution pH 7 and 9 (such as shown in Figure 2c, d) are further investigated. To understand these kinds of profiles, we take a closer look at the guest–guest and guest–host interactions identified in the previous section and their effect on the filling of the zeolite. The zeolite crystals are first incubated in water, and an aqueous resorufin solution is added at time = 0 min. The resorufin diffusion into two zeolite-β crystals at an external pH 7 and 9 is shown in Figure 5a. We represent the intensity profile through the crystals' center with a kymograph (Figure 5b, c), and the intensity profile at a quarter relative position is plotted in Figure 5d. Here, a fast rise followed by a slower decay of the fluorescence intensity describes both profiles. However, the intensity peaks later and the rates of the rise and decay are lower at an external pH 7.

The filling behavior provides insight into guest–guest and guest–host interactions. The concentration profile of resor-
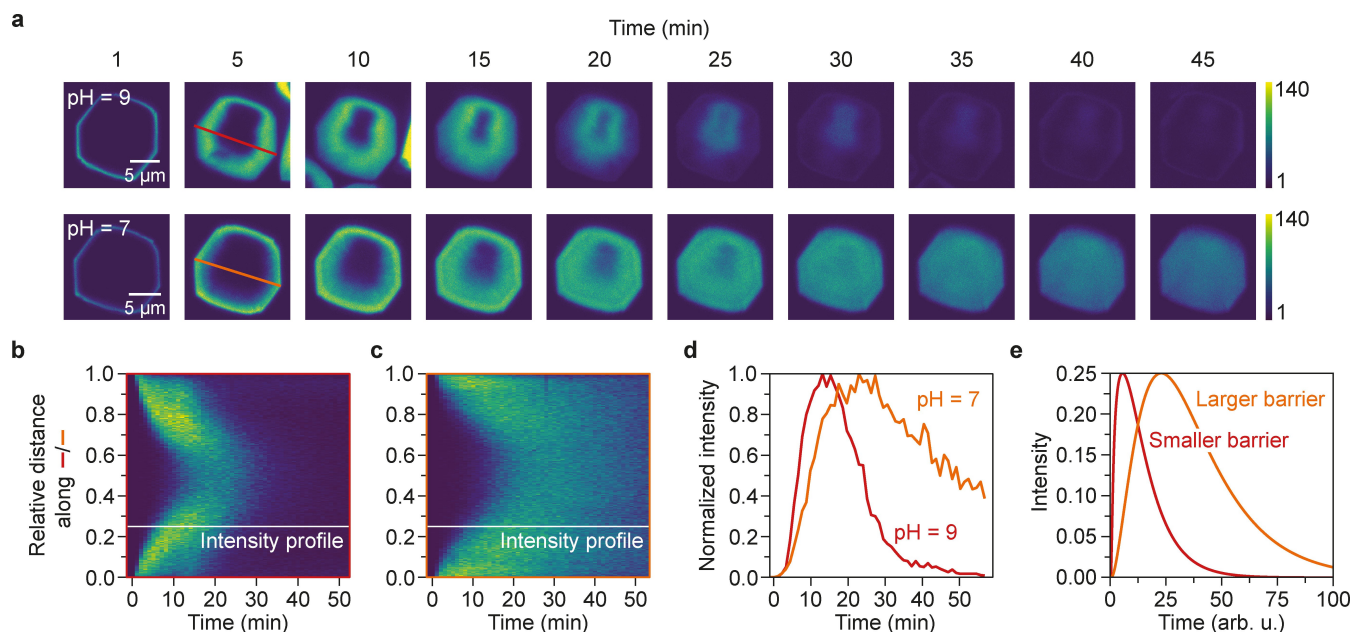
Chemistry–A European Journal

Research Article
doi.org/10.1002/chem.202302553

Chemistry
Europe
European Chemical
Societies Publishing

Figure 5. a) Confocal laser scanning microscopy micrographs of H-zeolite-β crystals incubated in water followed by incubation in 50 μM resorufin at two external pH values ($\lambda_{ex} = 493$ nm) starting at time = 0. Kymographs along the red (b; pH 9) and orange (c; pH 7) solid lines marked in (a). d) Intensity profile at 25% of the relative position (white lines in b and c) under pH 9 and 7 conditions. e) Simulated intensity profile at 25% of the relative position of protonated resorufin corrected for J-aggregation computed with a 1D diffusion model that accounts for a diffusion barrier.

ufin and ammonia inside the zeolite is computed over time with a diffusion model. From this, we calculate an intensity profile by either considering aggregation-induced quenching or deprotonation of ResH as a function of the modelled local pH. Here, we assume that all fluorescence originated from ResH. Then, the simulated and experimental kymographs are compared to find the dominant guest–guest and guest–host interactions.

Most likely is the scenario where the fluorescence intensity is quenched at increasing resorufin concentration due to J-aggregation of the molecules (see comparison scenarios in Section S6). The fluorescence intensity $I(x, t)$ is assumed to be proportional to the ResH concentration $c(x, t)$ minus a quadratic term accounting for aggregation-induced quenching,

$$I_{J-aggregation}(x, t) \propto c(x, t) - Ac(x, t)^2 \qquad (1)$$

with A being a proportionality constant. The intensity profile matches the shape of the experimental profile well both at pH 7 and 9 (Figure 5e). We conjecture that a higher concentration of ResH aggregates in solution at pH 7 might block surface pore openings, thereby increasing the surface barrier. This leads to the stretching of the intensity profiles as observed in the experiment. Variations in the surface barrier of individual zeolites crystals from the same synthesis have been reported.[36,37] This can account for the observed variations in the shape of the profile between crystals from the same synthesis batch.

To maintain a high emission intensity, even at high dye loading and/or basic conditions, we use a pH 7.4 HEPES buffer

to quench guest–host and guest–guest interactions (see demonstration and discussion in Section S7.1). HEPES can mitigate changes in local pH as well as J-aggregation. First, HEPES is a pH-buffer molecule that keeps the pH constant around 7, where resorufin deprotonation occurs only slowly. Second, the relatively high concentration of HEPES molecules (250× higher than resorufin in solution) can serve as a spacer between resorufin molecules, preventing J-aggregation. These conditions are employed to visualize accessibility—and later diffusion—in the hierarchical and anisotropic pore structure of zeolite-β crystals.

Pore space of zeolite-β mapped with resorufin

The accessibility and diffusion are visualized in the hierarchical and anisotropic pore structure of zeolite-β crystals. We observe strong variations in the ResH fluorescence intensity from different zeolite crystals incubated for 5 days (Figure 6a), despite the homogeneous appearance of the zeolite crystals in scanning electron microscopy (SEM). The filling is in most cases homogenous, and resorufin staining reveals that the micropore structure is accessible throughout the whole crystal (Figure 6b). The intensity is lower at the interface between the subunits (Figure 6c). This demonstrates that these regions do not contain a microporous structure and allow for ResH H-aggregation or have a lower accessibility.[38] We use rhodamine 110 (Figure 6g) complementary to resorufin to visualize non-microporous defect voids because it does not fit inside the zeolite's micropores.[20,39] These defect voids make up a *secondary* pore space, which together with the micropores form a hierarchical
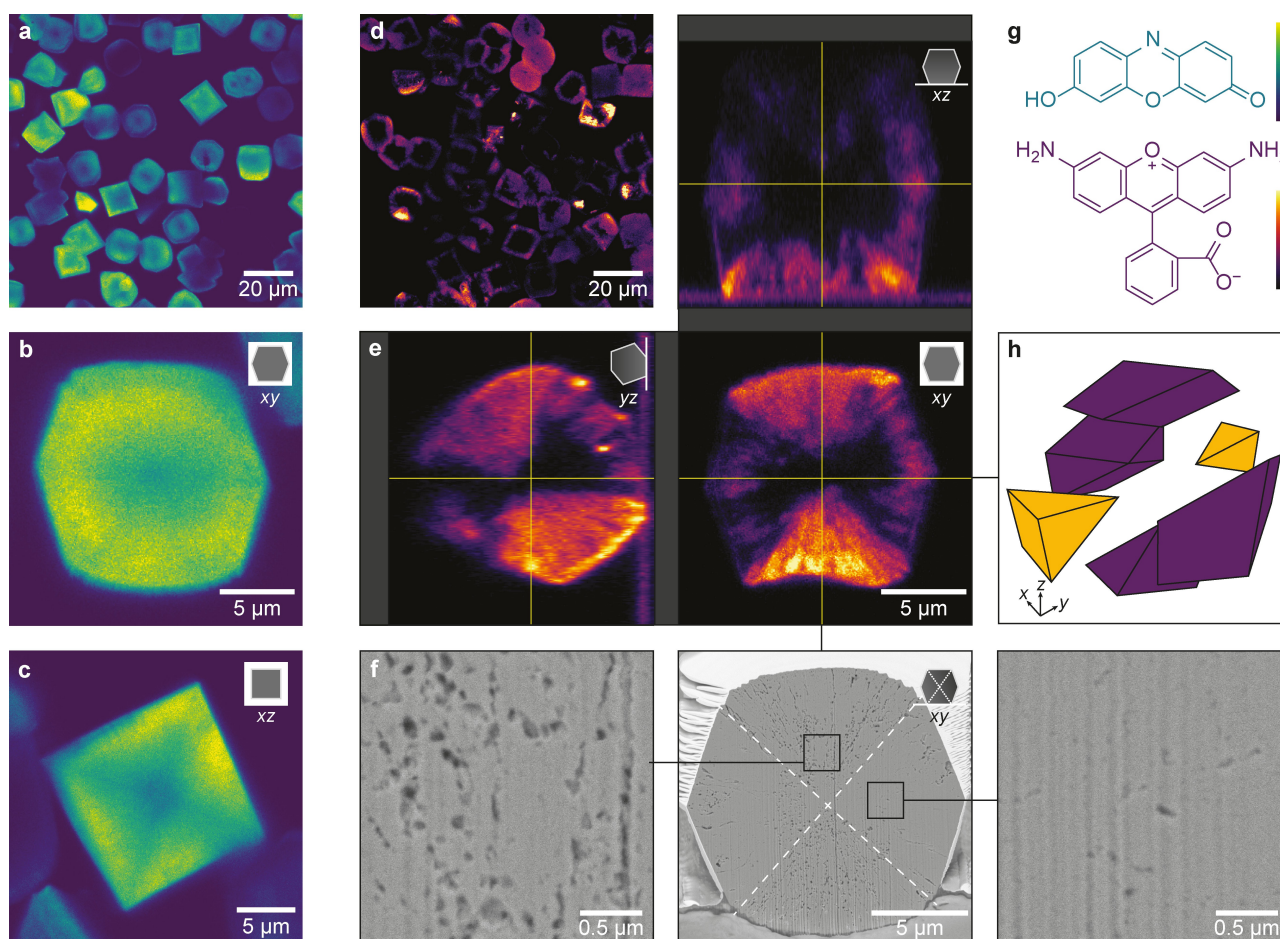
Figure 6. Confocal laser scanning microscopy micrographs of H-zeolite-β crystals incubated for 5 days in a)–c) resorufin in 12.5 mM HEPES (pH 7.4, $\lambda_{ex} = 493$ nm) and d), e) rhodamine 110 solution. A strong inter-crystal heterogeneity is apparent in the zoomed-out micrographs (a) and (d). Most crystals are filled homogeneously with resorufin (b). The boundaries between the crystal subunits can sometimes be discerned (c). Orthogonal cross sections through the center of the same crystal with the cartoon indicating the crystal orientation (e). f) Focused ion beam-scanning electron microscopy cross section shows the meso- and macropore structure. The dotted lines indicate the subunit boundaries, and the black boxes indicate the magnified regions in the pyramidal (left) and side (right) subunits. Rhodamine 110 does not fit into the zeolite's micropores and mostly stains the pyramidal subunits (e) because of their higher meso- and macroporosity (f). g) Chemical structures of protonated resorufin (top) and rhodamine 110 at neutral pH (bottom).[44] h) Exploded view of zeolite-β and its subunits with the pyramidal subunits marked in yellow and side subunits marked in purple.

pore structure. We find a strong heterogeneity in the accessible secondary pore space, ranging from crystals with a secondary pore structure only at the edges to a fully permeated network (Figure 6d). The pyramidal subunits, which are marked yellow in Figure 6h, in many cases have an elaborate accessible secondary pore structure (Figure 6e). Recent crystal-growth simulations confirmed that the pyramidal subunits are highly defective.[40–42] Most of the secondary pores fan out from the center all the way to the outer surface. We conjecture that these pores are formed from defects in an early stage of the crystal growth and propagate in the growth direction.[43] Focused ion beam (FIB)-SEM of a cut through the center crystal plane reveals that the density of meso- and macropores is significantly higher in the pyramidal subunits than in other regions (Figure 6f). This shows that the higher density of these pores results in a more interconnected secondary pore network.

Diffusion of resorufin/HEPES in zeolite-β

We demonstrate that ResH can be used as a probe to visualize mass transport at the single-crystal level without background contributions from the surrounding solution, which provides good contrast in the early stages of diffusion. Snapshots from a time-lapse microscopy video of ResH diffusion into a large zeolite-β crystal are shown in Figure 7a. Resorufin preferentially enters the crystal through the side edges via the exposed straight channels as marked by the white arrows in Figure 7b (i.e., crystallographic a- and b-axes in Figure 6h). The van der Waals diameter of resorufin (7.3 Å) is slightly larger than the size of the straight pores (6.7 Å), which are known to accommodate molecules with dimensions larger than their pore opening.[10,11,45] The observed diffusion anisotropy is in line with our understanding of the pore structure that the "sinusoidal" pore openings are exposed at the surface of the pyramidal subunits (Figure S4). Resorufin is 1.7 Å larger than the sinusoidal pore openings (5.6 Å in polymorph A) and is not
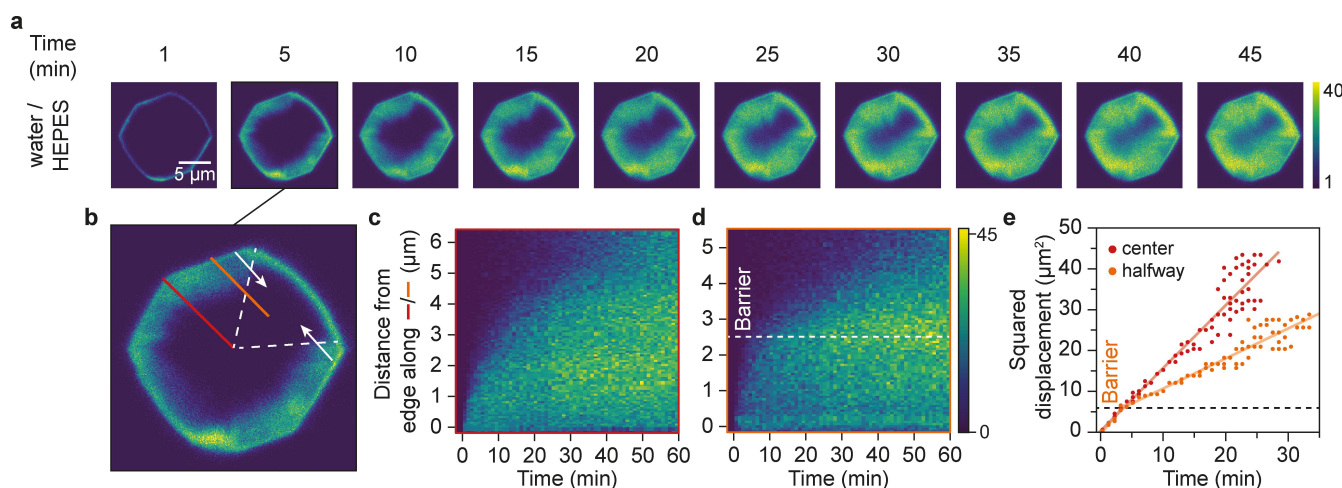
Chemistry–A European Journal

Research Article
doi.org/10.1002/chem.202302553

Chemistry Europe
European Chemical
Societies Publishing

Figure 7. a) Confocal laser scanning microscopy micrographs of a H-zeolite-β crystal in water followed by incubation in 50 μM resorufin in 12.5 mM HEPES (pH 7.4, $\lambda_{ex} = 493$ nm) starting at time = 0. b) After 5 min of incubation in resorufin solution, it becomes apparent that the diffusion is along the direction of the straight channels (white arrows) and is hindered by the inter-subunit boundaries (white dashed lines). Kymographs along the *red* "center" (c) and *orange* "halfway" (d) solid lines marked in (b). e) Squared displacement of the diffusion front along the "center" and "halfway" positions (dots); fits (solid lines) serve as guides to the eye. The subunit boundary is indicated by the dashed horizontal line in both (d) and (e).

likely to diffuse through—even when considering the random pore geometry in the disordered zeolite-β; this explains the negligible diffusion along the direction of these pores.[10,11]

The subunit boundaries impede diffusion along the direction of the straight pores, as evidenced by the clear diffusion front along this line.[38,41,46] To visualize the diffusion barrier more clearly, Figure 7c, d shows the intensity profile along two lines parallel to the straight channels as a function of time.[43] Figure 7c traces the red line of Figure 7b, which avoids the subunit boundaries, while Figure 7d traces the orange line of Figure 7b, which crosses such boundary. Until the ResH molecules reach the boundary, the filling proceeds similarly along both lines. The subunit boundary at 2.5 μm distance from the crystal surface (Figure 7d) slows down the filling as a result of the imposed diffusion resistance (Figure 7e and discussion in Section S7.2).[38] Figure 7a, b reveals that the diffusion front is ragged with spikes towards the crystal's center, following the direction of the secondary pore network towards the crystal's center. However, a large diffusion improvement in the direction of the secondary pore network in the pyramidal subunits is not observed. Large enhancements have been reported in hierarchical zeolites with an elaborate secondary pore network, provided that the network was interconnected along the diffusion direction.[47,48] We suspect that the secondary pore network in our samples is not sufficiently interconnected to facilitate large diffusion enhancements.

We showcase the quantitative analysis of the diffusion along the straight channels via kymograph analysis. The kymograph shown in Figure 7c is taken for diffusion coefficient estimation. We fit the first 15 min of the kymograph to prevent contributions from resorufin diffusing in from out-of-plane directions. Some parts of the zeolite have a higher brightness after filling than others. To reduce this effect, we normalize the intensity to the equilibrium profile at 60 min (Figure 8a). We fitted the kymograph to the well-known solution of Fick's second law

assuming a constant source of resorufin molecules diffusing in from one end, which models the excess of resorufin molecules in solution, and a concentration-independent diffusion coefficient D, that is,

$$\frac{c(x,t)}{c_0} = 1 - \text{erf}\left(\frac{x}{2\sqrt{Dt}}\right) \qquad (2)$$

with c the resorufin concentration, c_0 the resorufin concentration at the source, x the distance from the source, and t the time after exposure to the source. We assume that the measured intensity I is directly proportional to the local resorufin concentration $I_{normal}(x,t) \propto c(x,t)$ fitted with Equation (2). The normal diffusion model and residuals of the fit are shown in Figure 8b, c. A diffusion coefficient of 7×10^{-15} m^2 s^{-1} is found for this crystal. The normal diffusion model is not able to fully describe the kymograph. The model underestimates the measured intensity in the domain indicated by the white arrow in the residuals plot (Figure 8c). We investigate whether this could be the result of aggregation-induced fluorescence quenching due to J-aggregation. Following our findings, we include aggregation-induced quenching in the model using Equation (1). The J-aggregation model and residuals of the fit are shown in Figure 8d, e. The J-aggregation model describes the measured intensity better than the normal diffusion model, as evidenced by the residuals closer to zero (Figure 8e). A diffusion coefficient of 3×10^{-15} m^2 s^{-1} is found for this crystal, which is significantly lower than 7×10^{-15} m^2 s^{-1} found with the normal diffusion model. This analysis shows the importance of the guest–host and guest–guest interactions for diffusion coefficient estimation.
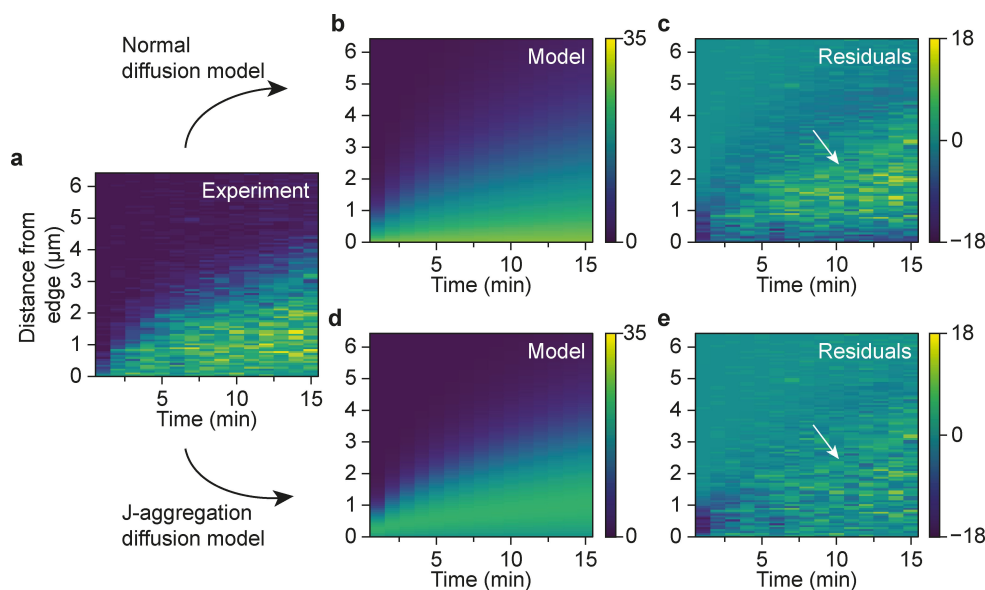
Chemistry–A European Journal

Research Article
doi.org/10.1002/chem.202302553

Chemistry Europe
European Chemical
Societies Publishing

Figure 8. a) Kymograph along red solid line marked in ("center" position in Figure 7b) cropped and normalized to last five frames of the full range of Figure 7c. Normal diffusion model fit to (a) plotted in the same false color scale (b) and its residuals (c). J-aggregation diffusion model fit to (a) plotted in the same false color scale (d) and its residuals (e). The aggregation diffusion model has smaller residuals, particularly in the domain marked by the white arrows.

Conclusions

We have found that—contrary to current understanding—the protonated form of resorufin is a viable fluorescent probe. Inside a zeolite, H-aggregation-induced fluorescence quenching was largely suppressed and protonated resorufin was stabilized, resulting in a bright fluorescence. Our results indicated that J-aggregation occurs within the zeolite pores at high resorufin concentration. Moreover, the solution pH affected both the dissociation state of resorufin inside the zeolite pores and the rate of entrance into the zeolite. We directly visualized anisotropic diffusion through the straight pores of zeolite-β and found a diffusion coefficient of 3×10^{-15} m^2 s^{-1}. Moreover, we directly showed the diffusion barrier imposed by the zeolite's subunit boundaries. In contrast to interference microscopy and infrared microimaging, our approach allows rapid and direct visualization of diffusion in microporous crystals with complex shapes. Analysis is straightforward, as the diffusion can be readily analyzed without the need for simulations to estimate the concentration profile as a two-dimensional projection. The small size of the resorufin probe makes it uniquely placed to investigate the accessibility, diffusion (barriers), and possibly even the local pH in zeolites and other microporous materials. Regarding the latter, it is important to recall that there is a vast literature on host–guest chemistry regarding transition metal ion complexes already illustrating that the local pH within zeolite cages and channels is different from what is expected based on aqueous solution chemistry.[49–51] Local probes, such as (protonated) dyes as well as the coordination spheres of transition metal ion complexes, could help in determining (changes in) the protonation chemistry within the confined spaces of porous inorganic materials, including zeolites and clay minerals.

Supporting Information

Details of the experimental methods, data analysis, and supplementary experiments (PDF) as well as a time-lapse movie of the data shown in Figure 7a (AVI) may be found in the Supporting Information. The authors have also cited additional references here.[52–79]

Conflict of Interests

The authors declare no conflict of interest.

Data Availability Statement

The data that support the findings of this study are available from the corresponding author upon reasonable request.

[1] G. Bellussi, A. Carati, R. Millini, in *Zeolites and Catalysis: Synthesis, Reactions and Applications* (Eds.: J. Čejka, A. Corma, S. Zones), Wiley-VCH, Weinheim, **2010**, pp. 449–491.

[2] T. De Baerdemaeker, B. Yilmaz, U. Müller, M. Feyen, F.-S. Xiao, W. Zhang, T. Tatsumi, H. Gies, X. Bao, D. De Vos, *J. Catal.* **2013**, *308*, 73–81.

[3] S. H. Van Vreeswijk, B. M. Weckhuysen, *Nat. Sci. Rev.* **2022**, *9*, nwac047.

[4] T. C. T. Pham, H. S. Kim, K. B. Yoon, *Science* **2011**, *334*, 1533–1538.

[5] S. Van Minnebruggen, T. De Baerdemaeker, K. Y. Cheung, A.-N. Parvulescu, U. Müller, P. Tomkins, R. de de Oliveira-Silva, X. Meng, F.-S. Xiao, T. Yokoi, W. Zhang, D. Sakellariou, D. De Vos, *J. Catal.* **2022**, *406*, 206–212.

[6] J. Kärger, D. M. Ruthven, D. N. Theodorou, *Diffusion in Nanoporous Materials* Wiley-VCH, Weinheim, **2012**, pp. 1–24.

[7] J. J. E. Maris, D. Fu, F. Meirer, B. M. Weckhuysen, *Adsorption* **2021**, *27*, 423–452.

[8] B. Dong, N. Mansour, T.-X. Huang, W. Huang, N. Fang, *Chem. Soc. Rev.* **2021**, *50*, 6483–6506.

[9] T. Lebold, J. Michaelis, C. Bräuchle, *Phys. Chem. Chem. Phys.* **2011**, *13*, 5017–5033.

[10] C. Baerlocher, L. B. McCusker, D. Olson, W. M. Meier, *Atlas of Zeolite Framework Types*, Published on Behalf of the Structure Commission of the International Zeolite Association by Elsevier, Amsterdam, **2007**, pp. 72, 73, 381.

[11] International Zeolite Association, *Database of Zeolite Structures*, http://www.iza-structure.org/databases/ (accessed 29–06–2023).

[12] A. Corma, M. T. Navarro, F. Rey, J. Rius, S. Valencia, *Angew. Chem. Int. Ed.* **2001**, *40*, 2277–2280.

[13] A. Corma, M. T. Navarro, F. Rey, S. Valencia, *Chem. Commun.* **2001**, 1486–1487.

[14] J. M. Newsam, M. M. J. Treacy, W. T. Koetsier, *Proc. R. Soc. Lond. A* C. B. De Gruyter, **1988**, *420*, 375–405.

[15] J. B. Higgins, R. B. LaPierre, J. L. Schlenker, A. C. Rohrman, J. D. Wood, G. T. Kerr, W. J. Rohrbaugh, *Zeolites* **1988**, *8*, 446–452.

[16] J. Kärger, T. Binder, C. Chmelik, F. Hibbe, H. Krautscheid, R. Krishna, J. Weitkamp, *Nat. Mater.* **2014**, *13*, 333–343.

[17] C. Chmelik, R. Gläser, J. Haase, S. Hwang, J. Kärger, *Adsorption* **2021**, *27*, 819–840.

[18] R. Kumarasinghe, E. D. Higgins, T. Ito, D. A. Higgins, *J. Phys. Chem. C.* **2016**, *120*, 715–723.

[19] Z. Zhujun, W. R. Seitz, *Anal. Chim. Acta* **1984**, *160*, 47–55.

[20] C. Seebacher, J. Rau, F.-W. Deeg, C. Bräuchle, S. Altmaier, R. Jäger, P. Behrens, *Adv. Mater.* **2001**, *13*, 1374–1377.

[21] S. Han, T. M. Hermans, P. E. Fuller, Y. Wei, B. A. Grzybowski, *Angew. Chem. Int. Ed.* **2012**, *51*, 2662–2666.

[22] L. Tian, H. Feng, Z. Dai, R. Zhang, *J. Mater. Chem. B.* **2021**, *9*, 53–79.

[23] P. Chen, X. Zhou, H. Shen, N. M. Andoy, K.-S. Han, G. Liu, W. Meng, *Chem. Soc. Rev.* **2010**, *39*, 4560–4570.

[24] N. Zou, X. Zhou, G. Chen, N. M. Andoy, W. Jung, G. Liu, P. Chen, *Nat. Chem.* **2018**, *10*, 607–614.

[25] B. Dong, Y. Pei, F. Zhao, T. W. Goh, Z. Qi, C. Xiao, K. Chen, W. Huang, N. Fang, *Nat. Catal.* **2018**, *1*, 135–140.

[26] B. Dong, N. Mansour, Y. Pei, Z. Wang, T. Huang, S. L. Filbrun, M. Chen, X. Cheng, M. Pruski, W. Huang, N. Fang, *J. Am. Chem. Soc.* **2020**, *142*, 13305–13309.

[27] B. Dong, Y. Pei, N. Mansour, X. Lu, K. Yang, W. Huang, N. Fang, *Nat. Commun.* **2019**, *10*, 4815.

[28] C. Bueno, M. L. Villegas, S. G. Bertolotti, C. M. Previtali, M. G. Neumann, M. V. Encinas, *J. Photochem. Photobiol.* **2002**, *76*, 385–390.

[29] A. G. Ryder, S. Power, T. J. Glynn *in Opto-Ireland 2002: Optics and Photonics Technologies and Applications* International Society for Optics and Photonics, **2003**, pp. 827–835.

[30] D. J. Coleman, D. A. Kuntz, M. Venkatesan, G. M. Cook, S. P. Williamson, D. R. Rose, J. J. Naleway, *Anal. Biochem.* **2010**, *399*, 7–12.

[31] L. Flamigni, E. Venuti, N. Camaioni, F. Barigelletti, *J. Chem. Soc. Faraday Trans. 2* **1989**, *85*, 1935–1943.

[32] N. Alarcos, B. Cohen, M. Ziółek, A. Douhal, *Chem. Rev.* **2017**, *117*, 13639–13720.

[33] V. Martinez-Martinez, R. Garcia, L. Gomez-Hortigüela, J. Perez-Pariente, I. Lopez-Arbeloa, *Chem. Eur. J.* **2013**, *19*, 9859–9865.

[34] D. Brühwiler, N. Gfeller, G. Calzaferri, *J. Phys. Chem. B.* **1998**, *102*, 2923–2929.

[35] Y. Jiao, B. Zhu, J. Chen, X. Duan, *Theranostics* **2015**, *5*, 173–187.

[36] J. Kärger, H. Pfeifer, R. Richter, H. Fürtig, W. Roscher, Rüd Seidel, *AIChE J.* **1988**, *34*, 1185–1189.

[37] J. C. S. Remi, A. Lauerer, C. Chmelik, I. Vandendael, H. Terryn, G. V. Baron, J. F. M. Denayer, J. Kärger, *Nat. Mater.* **2016**, *15*, 401–406.

[38] L. Karwacki, M. H. F. Kox, D. A. Matthijs de Winter, M. R. Drury, J. D. Meeldijk, E. Stavitski, W. Schmidt, M. Mertens, P. Cubillas, N. John, A. Chan, N. Kahn, S. R. Bare, M. Anderson, J. Kornatowski, B. M. Weckhuysen, *Nat. Mater.* **2009**, *8*, 959–965.

[39] M. B. J. Roeffaers, R. Ameloot, M. Baruah, H. Uji-i, M. Bulut, G. De Cremer, U. Müller, P. A. Jacobs, J. Hofkens, B. F. Sels, D. E. De Vos, *J. Am. Chem. Soc.* **2008**, *130*, 5763–5772.

[40] M. Trueman, D. Akporiaye, M. W. Anderson, *Faraday Discuss.* **2022**, *235*, 343–361.

[41] F. C. Hendriks, J. E. Schmidt, J. A. Rombouts, K. Lammertsma, P. C. A. Bruijnincx, B. M. Weckhuysen, *Chem. Eur. J.* **2017**, *23*, 6305–6314.

[42] A. N. Parvulescu, D. Mores, E. Stavitski, C. M. Teodorescu, P. C. A. Bruijnincx, R. J. M. K. Gebbink, B. M. Weckhuysen, *J. Am. Chem. Soc.* **2010**, *132*, 10429–10439.

[43] J. Sun, G. Zhu, Y. Chen, J. Li, L. Wang, Y. Peng, H. Li, S. Qiu, *Microporous and Mesoporous Mater* **2007**, *102*, 242–248.

[44] V. Jeannot, J.-M. Salmon, M. Deumié, P. Viallet, *J. Histochem. Cytochem.* **1997**, *45*, 403–412.

[45] F. C. Hendriks, D. Valencia, P. C. A. Bruijnincx, B. M. Weckhuysen, *Phys. Chem. Chem. Phys.* **2017**, *19*, 1857–1867.

[46] O. Geier, S. Vasenkov, E. Lehmann, J. Kärger, U. Schemmert, R. A. Rakoczy, J. Weitkamp, *J. Phys. Chem. B.* **2001**, *105*, 10217–10222.

[47] P. Kortunov, S. Vasenkov, J. Kärger, R. Valiullin, P. Gottschalk, M. Fé Elía, M. Perez, M. Stöcker, B. Drescher, G. McElhiney, C. Berger, R. Gläser, J. Weitkamp, *J. Am. Chem. Soc.* **2005**, *127*, 13055–13059.

[48] M.-H. Sun, J. Zhou, Z.-Y. Hu, L.-H. Chen, L.-Y. Li, Y.-D. Wang, Z.-K. Xie, S. Turner, G. Van Tendeloo, T. Hasan, B.-L. Su, *Matter* **2020**, *3*, 1226–1245.

[49] W. J. Mortier, R. A. Schoonheydt, *Progress Solid State Chem.* **1985**, *16*, 1–125.

[50] R. A. Schoonheydt, B. M. Weckhuysen, *Phys. Chem. Chem. Phys.* **2009**, *11*, 2794–2798.

[51] J. G. Mesu, T. Visser, A. M. Beale, F. Soulimani, B. M. Weckhuysen, *Chem. Eur. J.* **2006**, *12*, 7167–7177.

[52] D. C. Harris, *Quantitative Chemical Analysis* W.H. Freeman and Company, New York, **2010**, pp. 162–235.

[53] H. Moosmüller, W. P. Arnott, *J. Air Waste Manag. Assoc.* **2009**, *59*, 1028–1031.

[54] J. Hutter, M. Iannuzzi, F. Schiffmann, J. Vande Vondele, *WIREs Comput. Mol. Sci.* **2014**, *4*, 15–25.

[55] G. Te Velde, F. M. Bickelhaupt, E. J. Baerends, C. Fonseca Guerra, S. J. A. van Gisbergen, J. G. Snijders, T. Ziegler, *J. Comput. Chem.* **2001**, *22*, 931–967.

[56] A. D. Becke, *J. Chem. Phys.* **1993**, *98*, 5648–5652.

[57] C. Lee, W. Yang, R. G. Parr, *Phys. Rev. B* **1988**, *37*, 785–789.

[58] S. Grimme, J. Antony, S. Ehrlich, H. Krieg, *J. Chem. Phys.* **2010**, *132*, 154104.

[59] E. Van Lenthe, E. J. Baerends, *J. Comput. Chem.* **2003**, *24*, 1142–1156.

[60] C. C. Pye, T. Ziegler, *Theor. Chem. Acc.* **1999**, *101*, 396–408.

[61] J. Vande Vondele, J. Hutter, *J. Chem. Phys.* **2007**, *127*, 114105.

[62] M. Krack, *Theor. Chem. Acc.* **2005**, *114*, 145–152.

[63] H. P. Langtangen, S. Linge, *Finite Difference Methods for Diffusion Processes* University of Oslo, Oslo, **2016**, pp. 2–11.

[64] Dissociation Constants of Inorganic Acids and Bases in *CRC Handbook of Chemistry and Physics* (Ed.: J. Rumble), CRC Press, Boca Raton, **2023** (Internet Version 2023).

[65] X. Liu, J. Cheng, X. Lu, R. Wang, *Phys. Chem. Chem. Phys.* **2014**, *16*, 26909–26916.

[66] M. Petitjean, *J. Chem. Inf. Comput. Sci.* **1992**, *32*, 331–337.

[67] M. Petitjean, *Appl. Algebra Eng. Commun. Comput.* **2012**, *23*, 151–164.

[68] B. Valeur, M. N. Berberan-Santos, *Molecular Fluorescence* Wiley-VCH, Weinheim, **2012**, pp. 53–74, 285–325.

[69] J. W. Dobrucki, U. Kubitscheck, in *Fluoresc. Microsc.* (Ed.: U. Kubitscheck), Wiley-VCH, Weinheim, **2017**, pp. 85–132.

[70] M. Wahl, PicoQuant, *Technical Notes* **2014**, 1–14.

[71] E. G. McRae, M. Kasha, in *Phys. Process. Radiat. Biol.* (Eds.: L. Augenstein, R. Mason, B. Rosenberg), Academic Press, New York, **1964**, pp. 23–42.

[72] M. Kasha, H. R. Rawls, M. A. El-Bayoumi, *Pure Appl. Chem.* **1965**, *11*, 371–392.

[73] G. Ya Guralchuk, I. K. Katrunov, R. S. Grynyov, A. V. Sorokin, S. L. Yefimova, I. A. Borovoy, Y. V. Malyukin, *J. Phys. Chem. C.* **2008**, *112*, 14762–14768.

[74] S. B. Anantharaman, J. Kohlbrecher, G. Rainò, S. Yakunin, T. Stöferle, J. Patel, M. Kovalenko, R. F. Mahrt, F. A. Nüesch, J. Heier, *Adv. Sci.* **2021**, *8*, 1903080.

[75] D. Avnir, V. R. Kaufman, R. Reisfeld, *J. Non-Cryst. Solids* **1985**, *74*, 395–406.

[76] M. Wang, G. L. Silva, B. A. Armitage, *J. Am. Chem. Soc.* **2000**, *122*, 9977–9986.

[77] J. Kärger, J. Caro, *J. Chem. Soc. Faraday Trans. 1* **1977**, *73*, 1363–1376.

[78] J. Kärger, D. M. Ruthven, *Zeolites* **1989**, *9*, 267–281.

[79] S. Vasenkov, W. Böhlmann, P. Galvosas, O. Geier, H. Liu, J. Kärger, *J. Phys. Chem. B.* **2001**, *105*, 5922–5927.

Version of record online: November 9, 2023